

Space- and Post-Flight Characterizations of Perovskite and Organic Solar Cells


Lennart K. Reb, Michael Böhmer, Benjamin Predeschly, Sebastian Grott, Christian L. Weindl, Goran I. Ivandekic, Renjun Guo, Lukas V. Spanier, Matthias Schwartzkopf, Andrei Chumakov, Christoph Dreißigacker, Roman Gernhäuser, Stephan V. Roth, Andreas Meyer, and Peter Müller-Buschbaum*

Perovskite and organic solar cells are promising for space applications for enabling higher specific powers or alternative deployment systems. However, terrestrial tests can only mimic space conditions to a certain extent. Herein, a detailed analysis of irradiation-dependent photovoltaic parameters of perovskite and organic solar cells exposed to space conditions during a suborbital flight is presented. In orbital altitudes, perovskite and organic solar cells reach power-conversion efficiencies of more than 13% and 6%, respectively. Based on postflight grazing-incidence small-angle and wide-angle X-ray scattering, the active layer morphology and crystalline structure of the returned space solar cells are studied and compared to those of reference solar cells that stayed in an inert atmosphere. Minor changes in the active layer morphology are induced by the sole transport, without causing significant performance loss. For the space solar cells, morphological changes are attributed to the flight experiment that includes rocket launch, spaceflight, and reentry, as well as short-terrestrial environment exposure before and after launch. In contrast, no significant changes to the crystalline phase are observed. The notable performance during flight and high active layer stability, especially of perovskite solar cells, are promising results for further steps toward an orbital demonstration.

1. Introduction

In recent years, tremendous progress in next-generation solar cells (SCs) has been made based on novel materials. The gain of understanding of kinetic processes in nanoassembling, of novel strategies for tuning charge transfer and charge transport, or surface defect passivation during thin-film processing add threefold to the improvements in quality of the final devices—performance, stability, and reproducibility. Thereby, the power conversion efficiency (PCE) of organic photovoltaics has been steadily increasing to 18.2% certified and recently reaching 19.3%. In comparison, for the highest perovskite SC, the certified laboratory efficiency is reported at 25.7%, which is comparable to silicon-based photovoltaics.^[1–4] Various optimizations in these hybrid photovoltaics, such as the introduction of new materials or new techniques of layer treatments, have made these PCE advances possible in a

L. K. Reb, B. Predeschly, S. Grott, C. L. Weindl, G. I. Ivandekic, R. Guo,^[+]
L. V. Spanier, P. Müller-Buschbaum
TUM School of Natural Sciences
Department of Physics, Chair for Functional Materials
Technical University of Munich
James-Frank-Str. 1, 85748 Garching, Germany
E-mail: muellerb@ph.tum.de

 The ORCID identification number(s) for the author(s) of this article can be found under <https://doi.org/10.1002/solr.202300043>.

^[+]Present address: Solar Energy Research Institution of Singapore, National University of Singapore, 7 Engineering Drive 1, 117574, Singapore

^[++]Present address: Institut Laue-Langevin, 71 avenue des Martyrs, 38042 Grenoble, France

© 2023 The Authors. Solar RRL published by Wiley-VCH GmbH. This is an open access article under the terms of the Creative Commons Attribution-NonCommercial License, which permits use, distribution and reproduction in any medium, provided the original work is properly cited and is not used for commercial purposes.

DOI: 10.1002/solr.202300043

M. Böhmer, R. Gernhäuser
TUM School of Natural Sciences
Department of Physics, Central Technology Laboratory
Technical University of Munich
James-Frank-Str. 1, 85748 Garching, Germany

M. Schwartzkopf, A. Chumakov, S. V. Roth
Deutsches Elektronen-Synchrotron DESY
Notkestr. 85, 22607 Hamburg, Germany

C. Dreißigacker, A. Meyer^[++]
Institut für Materialphysik im Weltraum
Deutsches Zentrum für Luft- und Raumfahrt (DLR)
Linder Höhe, 51147 Köln, Germany

S. V. Roth
Department of Fibre and Polymer Technology
KTH Royal Institute of Technology
Teknikringen 56-58, SE-100 44 Stockholm, Sweden

P. Müller-Buschbaum
Heinz Maier-Leibnitz Zentrum (MLZ)
Technical University of Munich
Lichtenbergstr. 1, 85748 Garching, Germany

relatively short time.^[5] For example, in the case of organic SCs, such massive progress within the last few years became possible due to newly synthesized polymers and small molecules. Also, novel concepts like ternary all-polymer SCs lifted the PCE to over 17%.^[6] Toward promising applications, an increase in device stability was achieved, and simple solution-processed UV-filter layers and protective buffer layers promoted projected lifetimes of decades in organic nonfullerene-acceptor SCs.^[7] In addition to the optimization of the fabrication process, as discussed before, also the upscaling of the process becomes more important for real-world applications of these devices. Today, inkjet printing, spray-coating, or slot-die coating are widely used and allow upscaling the devices to hundreds of cm².^[8–13] In a recent field test, a notably large stand-alone perovskite farm of an area of 4.5 m² composed of 11 × 11 cm² single panels with a total peak power exceeding 250 W operated for more than 8 months.^[14] This large farm retained around 80% of its initial power after that time, showing that novel material solar panels can not only be processed at large scales in an industry-compatible route but also that this process can create long-term stable SCs with highly promising payback times.

The wet-chemical processing of device fabrication also allows using ultra-thin flexible polymer substrates that are difficult to use for other SC technologies due to temperature requirements or additional expensive production steps. The final plastic-foil-based solar panels are genuinely flexible with bending radii of 1 mm or below, which opens up new application fields for ultra-thin (micrometer) solar energy harvesting in combination with colorful plastic foils for novel device integrations.^[15]

In addition to the considerable interest in the terrestrial use of SCs, inorganic SCs are also used in space for a long time.^[16] This naturally raises the question about the suitability of next-generation SCs for space applications, in particular for perovskite-based photovoltaics (PV).^[17] Unlike terrestrial applications, which commonly focus on PCE and peak power, space applications focus on power densities since weight matters in space due to the need to lift objects by launching rockets. Thus, fabrication methods and material systems that allow decreasing the overall mass of final solar panels can be a game changer—the thinner the SC device can be manufactured, the more power-per-weight will be rewarded. To quantify this measure, the power-per-weight or specific power has been introduced previously, that is, the electric power in Watts that can be achieved per gram of solar module under standard laboratory illumination conditions. The current state-of-the-art inorganic space PV consists of bendable, not flexible, III–V triple-junction GaInP/GaAs/GaInAs or silicon/germanium-based modules that operate various spacecrafts, satellites, or probes.^[18,19] These technologies reach power-per-weight values of 1–3 W g^{−1}.^[19] In this regard, there are power-per-weight values reported for perovskite and organic SCs deposited on μm-thin plastic foils that are a magnitude higher, attesting to a high specific-power potential.^[15,20–26] These values are reported for single-junction systems, but there are promising developments for flexible tandem SCs with higher PCE potential.^[26,27] However, these numbers are frequently based solely on the active area of the devices that are still not representative of the entire weight of an SC module or array, including mounting framework, attenuators, and small motors, and a design with enough mechanical support to withstand extreme vibrations and accelerations during a rocket launch.

Moreover, there are concerns that on the module level a change of the SC material from a comparably rigid and heavy silicon-based solar panel array into perovskite or organic materials, the reduction in weight is low compared to the potential loss of PCE after certain lifetimes. However, a disruptive technology does question the fundamental beliefs in the field's current state-of-the-art. For example, plastic-foil-based solar panels might go up to space in a rolled-up state that is unfolded and stabilized by simple inflation without additional framework or attenuators. There might be no further need for heat dissipation since thermal management is directly achieved if unfolding to a fan-like shape or using semitransparent modules.^[28] Thus, perovskite and organic SCs might develop their full potential only in the combination of device progress and novel deployment systems.

Before such developments in the engineering of deployment systems will turn relevant, the novel materials need to be better qualified for space use. When it comes to space conditions, SCs face a harsh environment with strong temperature cycles, hard UV irradiation from the extraterrestrial AM0 solar spectrum (136.6 mW cm^{−2}), cosmic particle irradiation, lack of gravity, and ultra-high vacuum conditions.^[29–31] All these conditions deviate significantly from the terrestrial conditions, which are commonly used in testing perovskite and organic SCs. However, in addition to classical SC testing, more extreme conditions were studied for several years, which in parts mimic a part of space conditions selectively. For example, there has been early work to test organic SCs in a simulated space environment under UV irradiation and vacuum with encouraging results due to the lack of oxygen radicals.^[32] Perovskite SCs were stabilized against UV irradiation by introducing a photon energy downshifting layer.^[33] Perovskite SCs survived high-energy proton irradiation and demonstrated a radiation hardness that exceeds the damage threshold of crystalline silicon SCs.^[34,35] However, simulating actual space conditions on Earth is challenging. For example, while various works attested outstanding radiation hardness for perovskite and organic SCs in laboratory simulations, real space conditions might differ.^[35–38] Recently, a new set of testing guidelines for the radiation hardness screening of perovskite SCs suggested an adaption of test protocols for the soft and thin materials by using lower-energy proton irradiation, in particular, to avoid triggering self-healing effects.^[39] Moreover, mixed halide mixed cation perovskite SCs operated under illumination stably in a nitrogen atmosphere, whereas in the vacuum they showed phase segregation after a timescale of around 1 h.^[40] An additive for homogeneous cation distribution in the precursor can retard the phase segregation in standard conditions, but its action in space vacuum is unknown.^[41] Arguably, the temperature differences in Earth's orbits put high thermal stress on the SC materials. In recent work, after 200 temperature cycles, perovskite SCs still maintain more than 90% of their initial PCE.^[42] Lately, Bautista et al. tested encapsulated perovskite SCs in different architectures under various simulated space conditions, finding that the Spiro-OMeTAD electron blocking layer degraded the SCs faster compared to a carbon-based blocking layer.^[43] Hughes et al. used a mesoporous carbon electrode, simultaneously acting as encapsulation to avoid this degradation pathway with high proton irradiation hardness.^[44] Therefore, continuing terrestrial tests mimicking space conditions will be required to gain a more in-depth understanding.

Parallel to these specialized terrestrial tests of SCs, experiments in near-space and space are also needed. Stratospheric balloon flights explored near-space conditions at altitudes of about 30 km and showed functionality and power generation for several hours when testing perovskite and organic SCs.^[45,46] In a recent stratospheric experiment, the diurnal behavior of perovskite SCs was tested and power densities of up to 12 mW cm^{-2} were reached after more than 10 h exposure to ambient conditions.^[47] These tests were very powerful, particularly for near-space applications of perovskite and organic SCs. Still, these near-space tests simulate selected environmental parameters of space, but they cannot demonstrate the complete functionality of the technology in space. Therefore, additional steps and different approaches are required to bring these novel SC types up to space and characterize them there. For this purpose, suborbital-sounding rockets are the ideal testing platform. They reach orbital altitudes of more than 200 km, that is, a complete leave of Earth's atmosphere, which comes along with all space conditions, while rate control systems create determinable and stable irradiation conditions onto the SCs. The respective microgravity time of several minutes during the rocket flight allows several subsequent measurement cycles of a single SC under varying illumination and temperature conditions. Despite the short duration in space, the strength of such rocket-based experiments is also testing the harsh launching conditions in combination with the transport and handling on Earth before the launch, rather than enabling long-term stability tests. Thereby, these sounding rocket experiments come closest to orbital missions, before going to a full orbital demonstration, for example, on satellites or the International Space Station. In contrast to orbital demonstrations, the payload including the SCs can be recovered in sounding rocket experiments. Conventional spaceflights do not plan reentry with subsequent recovery, apart from sample return options at the International Space Station that are hardly available. This advantage over orbital demonstrations allows studying the returned SCs and comparing them with reference SCs, which were not exposed to space or transport stress to reveal differences caused by exposure to the environment.

To enable the testing of SCs on a sounding rocket flight, the Müller-Buschbaum group developed the Organic and Hybrid SCs In Space (OHSCIS) module.^[48,49] Here, we provide detailed results obtained during the first-ever spaceflight of perovskite and organic SCs during the maiden flight of OHSCIS as part of MAPHEUS 8 campaign launched from Northern Sweden.^[48,49] To date, this is the first and only space experiment that reports on in-space and postflight characterization of emerging PV that reached orbital altitudes. Before and during launch and subsequent spaceflight, the OHSCIS module steadily collected *I*-*V* curves of the SCs, together with temperature- and light-sensor measurements. From the sensor data parallelization, we determined the individual solar irradiance evolution for each SC at each point of the microgravity phase precisely in previous work.^[50,51] Based on these developments, in the present study, we present a quantitative PCE analysis throughout the rocket flight and identify the influence of environmental conditions such as solar irradiance or temperature on photovoltaic performance parameters of perovskite and organic SCs. Correlations between solar irradiance and PV parameters can be identified, where the SCs behave similarly as known from terrestrial tests. Furthermore, we investigate the morphology and crystal structure of the space-probed SCs

using grazing-incidence small-angle and wide-angle X-Ray scattering (GISAXS/GIWAXS) and compare them with reference SCs. This is to our knowledge the first ever reported postspaceflight characterization in the literature. Thereby, we can identify changes in the morphology and crystal structure of the active layer of perovskite and organic SCs, which were exposed to traveling, terrestrial handling, the harsh rocket launch, space conditions, and the Earth's atmosphere reentry. The active layers of the space SCs change their nanometer morphology compared to the reference SCs that stayed in the nitrogen-filled glovebox or that traveled to Sweden inside nitrogen atmosphere. Interestingly, the sole travel-induced slight changes in the morphology, without preventing the SCs from stable operation in space. Furthermore, the crystalline phase of the SCs shows no significant change. These results demonstrate that no significant degradation can be attributed to the SCs during the time of space exposure. Thus, this first spaceflight attests perovskite and organic SCs promising performance and stability to pave their way to future space experiments.

2. Experiment and Dataset

The OHSCIS experiment^[49] harbors eight insertion modules that are arranged azimuthally at 45° . The SC substrates are fixed with aluminum masks that define the eight SC apertures to each 10 mm^2 . In the lower positions are perovskite solar modules, in particular, mixed organic lead mixed halide perovskite with planar SnO_2 and mesoporous TiO_2 (*m*- TiO_2) architectures in an alternating arrangement.^[52] In the upper positions are organic solar modules, where the bulk-heterojunction active layers of narrow bandgap PTB7-Th:PC₇₁BM and nonfullerene PBDB-T:ITIC small molecule acceptor alternate.^[53,54] The respective SC architectures are shown in the insets in **Figure 1**, the detailed fabrication process for all four SC types is described in our previous work.^[48] Each insertion module contains fused silica glass to protect the SCs from extreme drag-heat during supersonic ascent. Here, we note that apart from this heat protection and hence nonequilibrium temperature that we monitored with temperature sensors, the SCs are mounted in a vented space inside the rocket mantle and, therefore, do experience space conditions during their flight. The SCs are not specially sealed to maximize environmental exposure during the launch and short spaceflight.

In the measurement mode, a perovskite and organic SC *I*-*V* curve are recorded in parallel in around 5 s. To record potential hysteresis, a backward sweep follows the forward sweep, amounting to $\approx 10 \text{ s}$ duration for a single SC measurement. Since each SC module contains eight individual SCs and measures one after another, it takes around 80 s for measuring the entire module, that is, to complete one full cycle for each of the eight insertion modules.^[48] At any given point during the measurement time, one SC of each module is measured, resulting in 16 parallel SC measurements in the entire experiment. For each sweep, the open circuit voltage (V_{OC}), the short-circuit current density (j_{SC}), the fill factor (FF), and the PCE are determined. For each segment, the irradiance maximum-likelihood-estimate that is most time-synchronous with the half-time sweep is selected for the latter calculation.^[50] Here, we note that the solar irradiance values used from previous work are derived without the consideration of soot on the windows and, thus, are upper limits to

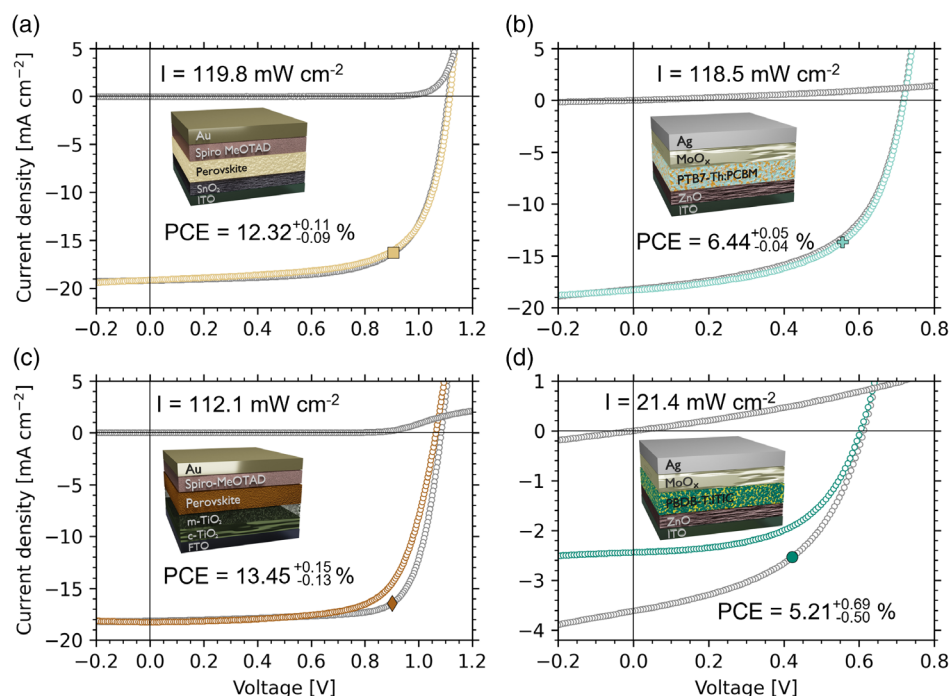


Figure 1. Current density–voltage curves in forward (colored circles) and backward (grey circles) directions that are used for calculating the champion power-conversion efficiencies measured during the spaceflight. The measurements shown for the four space solar cell architectures that are a) perovskite in planar SnO_2 , b) narrow bandgap PTB7-Th:PC₇₁BM bulk-heterojunction, c) perovskite in mesoporous TiO_2 , and d) PBDB-T:ITIC non-fullerene small molecule acceptor. The error bars are derived from the standard deviation of the solar irradiance determination. The simultaneous irradiance measurement during the sweep used for PCE calculation is denoted with the value I . The MPP is indicated with the large-filled symbol. Crossing the origin, the dark-current measurements before launch can be seen (gray curve). The insets show the respective device architectures.

the in-reality received somewhat lower solar power. Consequently, PCE values are conservative estimates throughout this work. The photovoltaic parameters presented and discussed in this work are extracted from the main measurement time, that is, the ≈ 6 min, while the rocket payload is on its parabolic trajectory outside Earth's atmosphere with stabilized orientation.

3. In-Flight Characterization

Relating the maximum power point (MPP) densities of the SC measurements to the irradiances determined during the respective voltage sweeps allows for deriving effective PCEs for the SCs. For this calculation, the fused silica glass is considered with ideal transmission apart from Fresnel reflection. This allows selecting the champion performance SC measurements in terms of their PCE.

In Figure 1, we present the resulting champion performances for each SC type on the rocket measured during the spaceflight. In addition to the forward and backward voltage sweep, the dark measurements of the very same cells prior to launch are shown. The highest PCEs for the different SC types in descending order are for the $m\text{-TiO}_2$ perovskite SCs 13.45% (Figure 1c), for the SnO_2 perovskite SCs 12.32% (Figure 1a), for the fullerene system 6.44% (Figure 1b), and the small-acceptor molecule 5.21% (Figure 1d). The irradiance value is stated in the figure together with errors given in the PCE determination corresponding to 1 σ

standard error from the uncertainty of the irradiance value. Most champion performance measurements occur at irradiances of more than 1000 W m^{-2} , which we define in accordance with terrestrial tests as 1 sun.

These values are calculated based on the assumption of a negligible absorption of the fused silica glass windows. However, during supersonic ascent, soot originating from the cork ablative nose-cone heatshield is deposited on the fused silica windows, thus effectively lowering the transmission through the glass. In Figure 2, we show photographs of one of the eight hatch windows after recovery. Figure 2d shows the glass window transmission of spatially distributed UV–vis slit positions. Interestingly, even in the glass regions where no visual absorption takes place, the UV transmission is strongly reduced, while the transmission in the optical range is reduced from Fresnel-limited transmission by around 5%. Hence, the cork soot acts as UV protection for the SCs behind the window as it preferentially reduces the transmission at lower wavelengths. The light attenuation becomes significant for the lower SC modules, which in this flight are all perovskite SCs. While the upper row of SCs experiences around 20% of effective irradiance decrease, the lower row only receives 1/2 to 1/3 of the possible solar irradiance. Here, we note that all high-performance SC data of the perovskite SCs are strictly derived from the upper row. We do not attempt to recalibrate for this soot effect since it is small for the organic SCs and the upper-row perovskite SCs. The pronounced edge of soot and the transmission gradient along the glass would make irradiance reconstruction more complex and

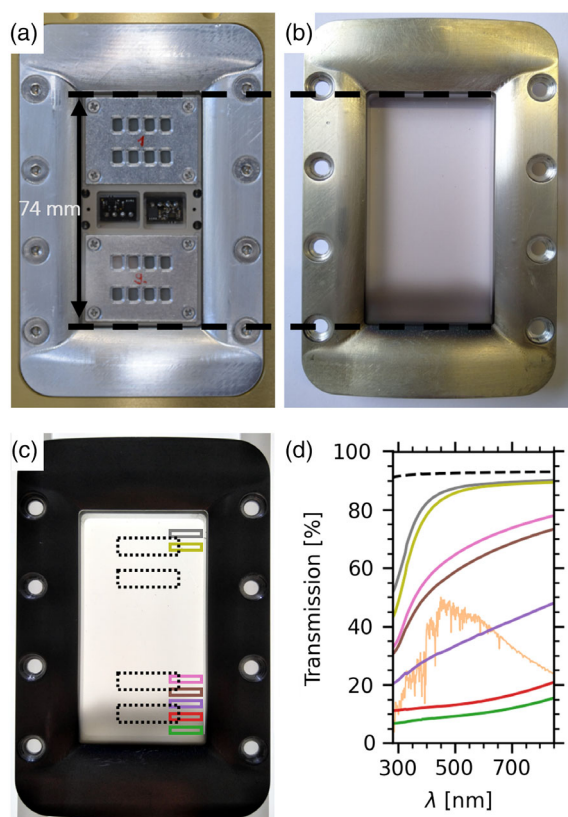


Figure 2. a–c) Photographs of the insertion module window, including the fused silica glass: a) The insertion module including SC aperture masks to show the exact position of the SC apertures relative to the window frame. b) Photograph of the recovered and disassembled insertion module. One can see soot deposited on the glass window's lower part, presumably dominantly deposited during supersonic ascent. The upper part of the window appears clear. c) Backlight illumination photograph of the same window to see the soot with a uniform contrast response. The four black-dotted rectangles indicate the approximate position of the rows of SC apertures (cf. a). The smaller colored rectangles depict the UV–vis slit size at various positions along the glass. The graph on the lower right shows the corresponding measured transmissions, where the black dashed line is the reference measurement of a clean glass. In addition, the AM0 solar spectrum is shown in arbitrary scale in orange.^[30,31] Note the dominant decrease of glass transmission in UV, where the glass appears clear in the photographs.

error-prone for inclined solar directions. Thus, the PCE stated in Figure 1 can be considered a conservative estimate of the real potential of the cells in the space environment and will be relatively higher.

A detailed SC parameter overview during the rocket flight can be found in Figure 3. A detailed table with computed Pearson correlation for SC parameter and irradiance is shown in Table S1, Supporting Information. The perovskite open-circuit voltage V_{OC} values lie around 1 V, reaching up to 1.1 V in phases of strongest solar illuminations, while the organic SCs show lower V_{OC} values with maximum values exceeding 0.7 V (Figure 3a). In phases of weak solar irradiance at around 250 s after lift-off, there is a notable decline of the V_{OC} values. Since

the solar irradiance varies over the rocket flight, the V_{OC} values are sorted as a function of the solar irradiance (Figure 3b). The histograms in the background of Figure 3b show the relative number of measurements performed at the respective irradiance values. There is a lack of data of measurements at around 0.8 sun. We chose 0.7 sun as a threshold for the tabulated Pearson correlation coefficients, which is below the sparsely sampled region at around 0.8 sun and above the threshold of any shadowing effects (as described in detail below). Therefore, the Pearson correlation values in the higher irradiance range in Table S1, Supporting Information, are not biased by shadowing influences. While the perovskite V_{OC} values increase steadily toward higher irradiances within the measurement range ($P_{<0.7} = 0.62$, $P_{>0.7} = 0.16$), the correlation for organic SCs holds only up to a threshold of around 0.6 suns ($P_{<0.7} = 0.42$). Consecutively, the V_{OC} values appear to level off and stay constant for the organic SCs ($P_{>0.7} = -0.05$). The same trend was found for perovskite and organic SCs on terrestrial field studies,^[55,56] indicating that the tested SCs behave in space as anticipated from terrestrial tests and no additional effects hit in. With the time of the spaceflight, the V_{OC} and FF values decline slightly (Figure S1, Supporting Information), which is correlated to increasing SC temperatures due to thermal conduction or radiation from the hot mantle surface to the SC holders. In this regard, the SCs show the same behavior as expected from the temperature-dependent detailed balance limit as is found for terrestrial test SCs, where also the V_{OC} -decrease is most pronounced upon temperature increase.^[55,57] In our dataset, the V_{OC} decrease upon temperature increase; however, it is not decoupled from changes in irradiance, which show a strong correlation in Figure 3b. Instead, the decline during the spaceflight is more pronounced for the FF, since the correlation between FF and irradiance appears not as strong in Figure S1, Supporting Information (no positive Pearson correlation). The FFs of perovskite SCs lie in the range of 60–75%, where the *m*-TiO₂ architecture SCs show a higher average than the ones with SnO₂, which follows the systematic trend that was already seen during precharacterization, where the former system showed higher PCE and larger FF values.^[48] The FF decrease over time is likely attributed to the steadily increasing temperatures measured at the SC positions during flight, particularly for the organic SCs. During the measurement time in vacuum, the outside facing temperatures increase from initially 30 to 50–55 °C at the end of the microgravity phase (Figure 3e). Since the temperature sensors are placed directly next to the SCs, we consider them to give reasonable indications of the actual temperature present for the SCs. The effect of solar irradiation warming up the outside temperature sensor when shining onto them is visible as additional bumps for some segments of the outside temperature evolutions. The reentry shock heats the temperature sensors at the windows to around 60 °C. The last measurements before the experiment shut off imply a stabilization of the temperatures with no further substantial warming.

The PCE analysis is done by relating the power density measurements at the MPP to the irradiance at that time and for that particular segment (Figure 3c). Here, we use the irradiance values from our previous work, which do not account for soot and thus should be considered as upper limits to the effective received solar power.^[50] Thus, the interpretation of the PCE

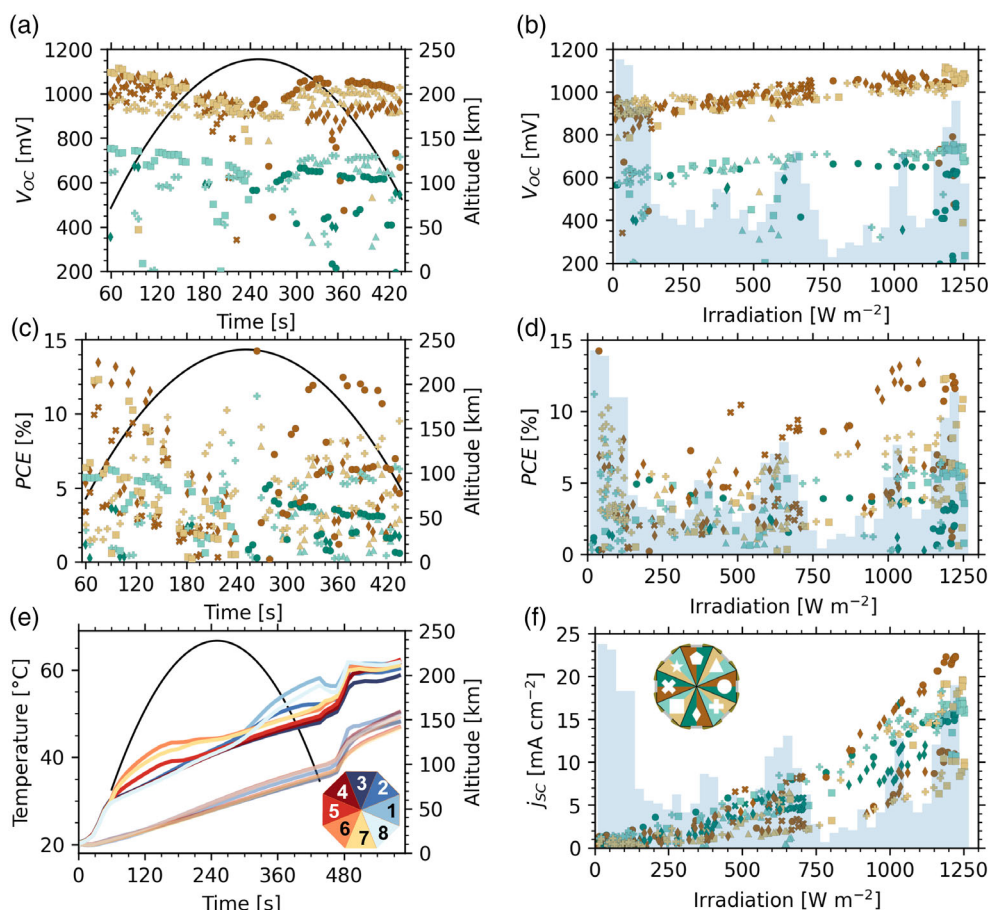


Figure 3. Overview of the SC parameter evolution during the spaceflight for perovskite (brown symbols) and organic (green symbols) SCs. The used colors and symbols correspond to the SC types and positions in the experiment as indicated in the inset in (f). a) V_{oc} as a function of time after LO (lift-off time of the rocket) shown together with the altitude above ground. b) V_{oc} as a function of irradiance. The blue background histogram indicates the relative number of measurements that could be performed at the respective irradiance, irradiances below 0.01 sun are excluded. Please refer to previous work for the irradiance evolution for each segment.^[50] c) PCE as a function of time after LO is shown together with the altitude above ground. d) PCE as a function of irradiance. The PCE values are conservative estimates as described in the text. e) Temperature measurements during flight shown together with the altitude above ground. The upper group of thicker lines is the average temperature from both sensors placed next to the SCs. The lower group of thinner lines are the average temperatures from inside the rocket of the bottom plate. The colored inset assigns the different temperature lines to the respective module. f) j_{sc} as a function of irradiance. Refer to Reb et al., 2020 for the j_{sc} evolution.^[48]

values should take the soot discussion above into account. The PCE evolution shows values from typically 6–13% for the perovskite SCs and 2–6% for organic SCs. There are outliers of higher efficiency in the phase of very low solar irradiance (below ≈ 0.1 sun) since a small absolute underestimation of solar irradiance at faint conditions is converted into a large relative underestimation that in turn biases the PCE to high values.^[50] This effect can be seen in detail in Figure 3d, where especially in the region below 0.1 sun, high efficiencies occur that should not be considered for further interpretation. Hence, we include only measurements above 0.15 sun into the Pearson statistics.

In the range between 0.1 and 0.4 sun, there is an underpopulation of well-performing SCs in terms of their PCE. This underrepresentation neither is seen in the V_{oc} values in Figure 3b nor in the FF values in Figure S7, Supporting Information, but instead in the j_{sc} values in Figure 3f. At these moderate irradiances, the solar inclination is still high and leads to a relative shift

of the illuminated area with respect to the active area of the SCs, as well as to geometrical shadowing effects due to the aperture mask, effectively reducing the current-generating area below the aperture size (see Figure S2, Supporting Information). Interestingly, this effect is strong enough to occur in the Pearson correlation coefficients, where for both perovskite and organic SCs the correlation is stronger above 0.7 sun. Apart from these moderate irradiance effects, there appears to be a slight nonlinearity in the j_{sc} s as a function of irradiance—for increasing irradiances, the j_{sc} values grow overproportionally also at higher irradiances (Figure 3f). Such a nonlinear dependency was not found for terrestrial tests for perovskite and organic SCs, where the current density was a linear function of irradiance.^[55,56] However, this visual trend should not be overinterpreted here since due to the unequal distribution of measurements as a function of irradiance and due to individual scattering of the j_{sc} values, errors could enter in and further tests will be required.

The effect of soot is best accessible in the sorted j_{sc} values as a function of irradiances (Figure 3f) for the perovskite SCs. There appear to be one upper and one lower branch of j_{sc} values, where the lower branch shows approximately half the current as compared to the upper branch, with not much scatter in between, underlining the high reproducibility of the perovskite SCs selected for the spaceflight.

We identify a trend for the perovskite SCs that PCE increases with increasing irradiances ($P_{0.15} < 0.51$), while this effect is not as pronounced for the organic SCs ($P_{0.15} < 0.36$).

An apparent increase in fluctuations of the PCE values compared to V_{oc} , j_{sc} , and FF can be explained by the attenuation influence of soot on the fused-silica windows. The presence of soot and the soot gradient in Figure 2 introduces a variable bias toward overestimating the received solar irradiance and hence an underestimation of the PCE values for all SCs. For example, the lower branch of the beforementioned j_{sc} measurements of perovskite SCs reaches only around 6% PCE, while these SCs are supposed to be equal to their conservative 12% PCE estimate counterparts with lower soot bias.

4. Postflight Characterization

The sounding rocket experiment enables a postflight characterization in addition to the in-flight SC studies. To assess potential

changes in the SCs due to the exposure to space during the rocket flight, including the harsh rocket launch with extreme accelerations and vibrations and rocket reentry with more than 20 g peak acceleration, studies of the morphology and crystal structure of the SCs are ideal. To investigate buried structures in thin film devices and to probe a statistically large sample volume, GISAXS and GIWAXS measurements were demonstrated to be extremely powerful.^[58,59] Accordingly, we performed GISAXS and GIWAXS measurements on the SCs that went to space and present the first postspaceflight characterization of organic and perovskite SCs. In this work, we focus on the active layer bulk morphology and structure by impinging above the material's critical angle as described in detail in the corresponding Experimental Section. For reference, GISAXS and GIWAXS measurements were also done on identical SCs that stayed in Munich inside the nitrogen-filled glovebox and SCs that traveled to Sweden in nitrogen-filled packages but were not exposed to space conditions or ambient air. Figure 4a shows the travel of the different SC groups. The sample storage procedure and environmental conditions apart from the rocket flight are detailed in the Experimental Section. In Figure 4b, exemplary GISAXS and GIWAXS measurements of an organic and a perovskite SC returned from space are shown, respectively.

To analyze the morphology of the SCs exposed to the rocket flight and compare it to the reference SCs, which traveled to Sweden or stayed in Munich instead of the Sweden travel, we

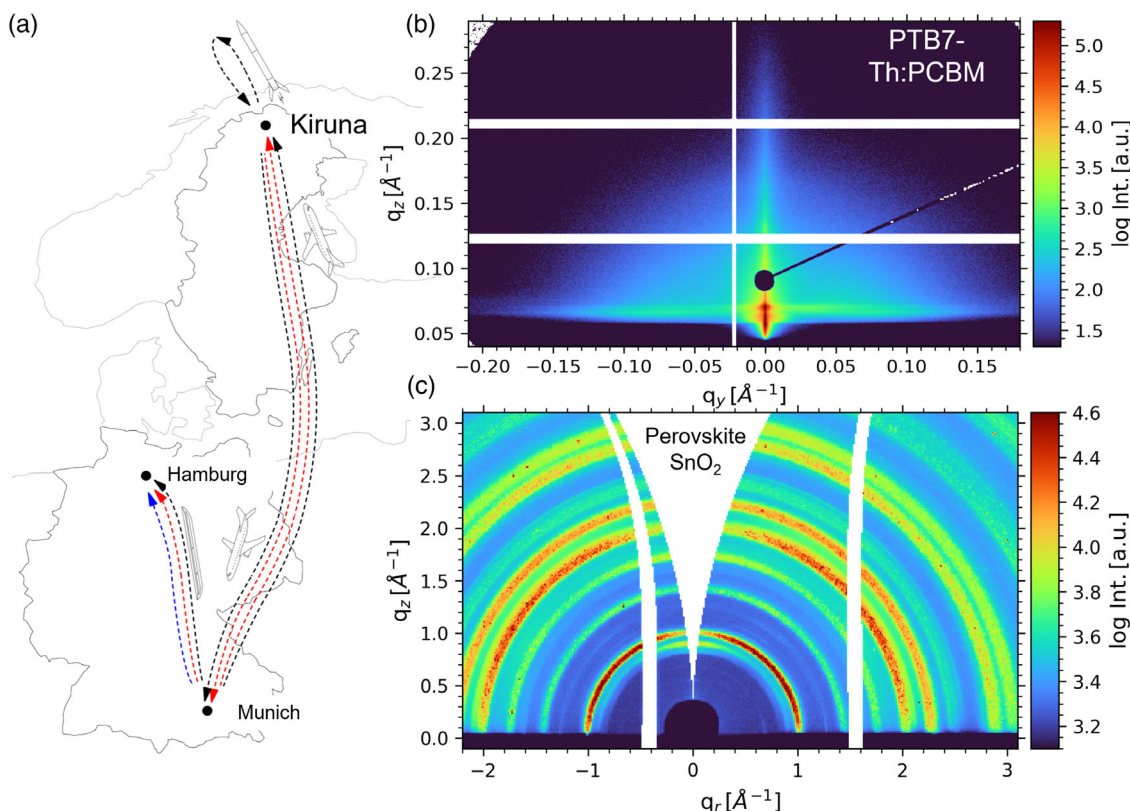


Figure 4. a) The travel paths of the three different SC groups: Munich reference SCs (blue), the Sweden reference SCs (red), and the SCs on the rocket flight (black). Exemplary b) GISAXS measurement of an organic rocket SC and c) GIWAXS measurement of a perovskite rocket SC, respectively. An overview of all the preprocessed 2D GISAXS and 2D GIWAXS data can be found in Figure S3 and S4, Supporting Information, respectively.

perform GISAXS and GIWAXS measurements on all four SC types (see Figure S3 and S4, Supporting Information, respectively). The resulting horizontal line cuts of the 2D GISAXS data performed at the critical angle of the respective active layer materials contain the lateral morphology information. When comparing the line cuts for one type of SC, which was exposed to different experimental conditions, moderate changes in scattering data can be found. To quantify these changes, the datasets are analyzed with fits (Figure 5) based on models as described in the Experimental Section. Since modeling with only two distinct object sizes (form factors) and distances (structure factors) did not result in good representations, we use three distinct object sizes and distances in the GISAXS data analysis. Moreover, the small-, medium-, and large-sized objects have a size distribution to account for their polydispersity. This way, the modeling results in data representations of acceptable quality. Here, we note that the complex physics of SAXS data in grazing-incidence mode are described with a model that includes simplifications and, hence, we do not expect the model to provide a perfect fit to the data. However, the modeling with three form and structure factors gives us the possibility to quantitatively assess the changes in the thin-film morphology of the active layers.

Due to the polydispersity taken into account in the data analysis, obtained fit results are best shown with the form factor size distributions and structure distances (Figure 6). Here, the counts represent the number of scattering objects for the given size and we note that the curves are not normalized. On the first view, the morphology of the SCs which stayed in Munich differs from those which traveled to Sweden and those which experienced

the spaceflight. Thus, the transport as well as the rocket flight cause changes in the morphology of the active layers in the nanoscale.

In more detail, for the planar SnO_2 perovskite SCs (Figure 6a), the small domains become smaller and increase in number from the Munich to the Sweden samples and the trend continues from Sweden to the space samples. For the mesoporous TiO_2 perovskite SCs (Figure 6b), an effectively similar trend occurs, however, the explanation approaches from the opposite direction. The large domains become less when going from the Munich samples to the Sweden samples and the trend continues for the space samples. In essence, both trends indicate a drive toward smaller domains of the domain size distribution. Interestingly, the spaceflight does not show a particularly strong influence. Instead, the change is comparable to the shift of the Sweden samples experienced without being exposed outside their protective nitrogen atmosphere.

For the organic SCs, the scenario is somewhat more complex. Table 1 lists the resulting sizes from the modeling as an additional overview. The PBT7-Th:PCBM active layer system (Figure 6c) experiences a moderate size growth but a relative number reduction of the medium-sized domains due to the travel to Sweden. The spaceflight does not alter the domain radii distribution in a broad range from 10 to 90 nm, while there is an increase in the typical distance of the large domains from Munich over Sweden to space. For the PBDB-T:ITIC active layer system (Figure 6d), large domains become smaller from Munich to Sweden but become larger from Sweden to space, the middle-size domains showing the same trend. However, these changes are mostly covered within the 1σ confidence interval and the

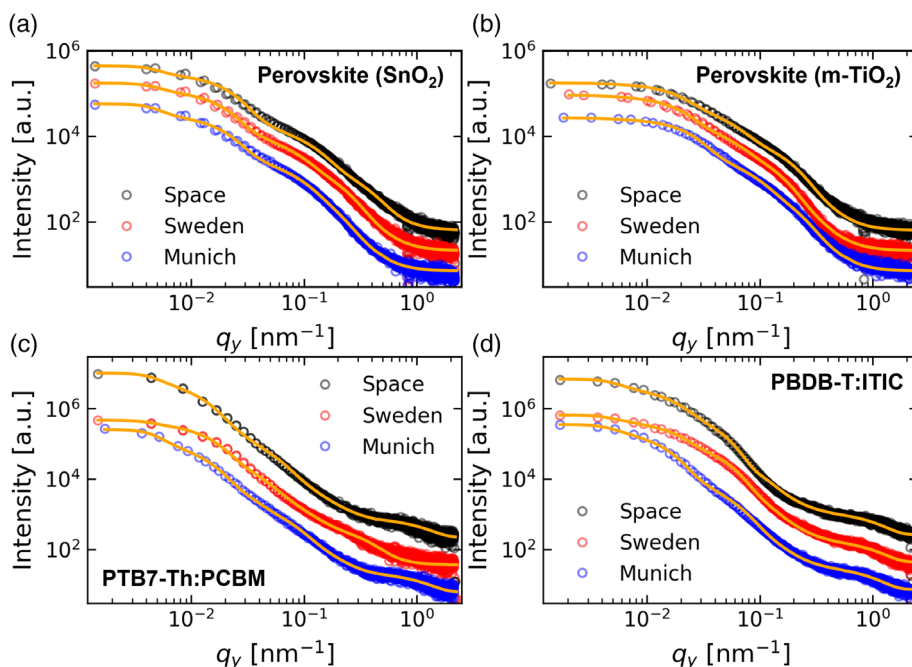


Figure 5. Horizontal line cuts of the 2D GISAXS data of SCs exposed to the spaceflight (black), SCs that traveled to Sweden (red), and SCs that stayed in Munich (blue) are shown together with the best model fits (solid lines): a) Planar SnO_2 perovskite SC, b) mesoporous TiO_2 perovskite SC, c) fullerene organic SC, and d) small-molecule acceptor organic SC.

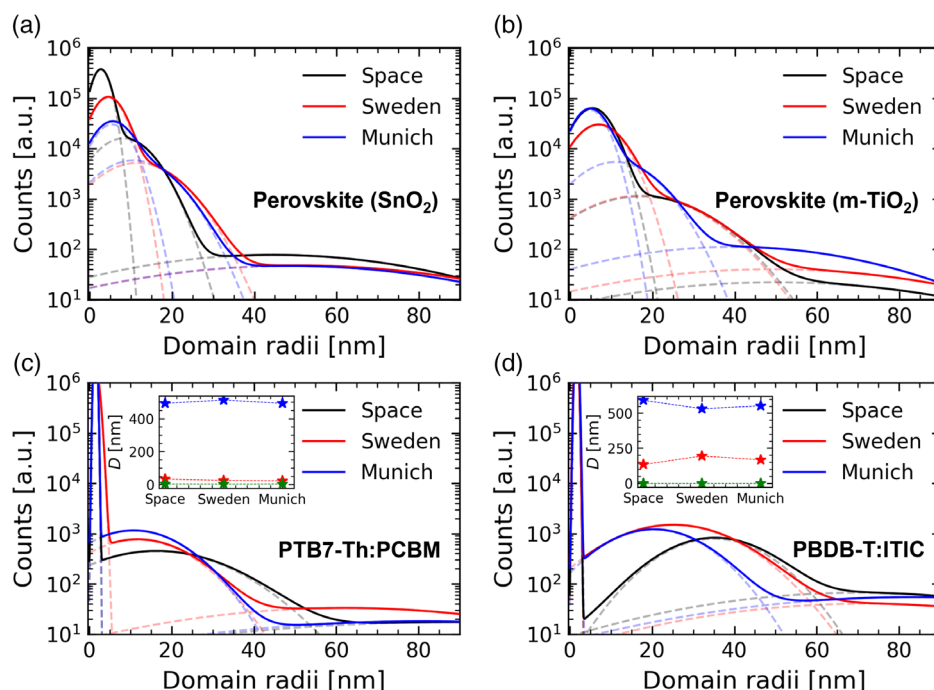


Figure 6. Domain size distributions of SCs exposed to the spaceflight (black), SCs that traveled to Sweden (red), and SCs that stayed in Munich (blue): a) Planar SnO_2 perovskite SC, b) mesoporous TiO_2 perovskite SC, c) fullerene organic SC, and d) small-molecule acceptor organic SC. The insets show the characteristic nearest neighbor distances of the large (D1), medium (D2), and small (D3) domains.

Table 1. Organic SC domain radii obtained from the GISAXS models. Uncertainties stated are derived from 1σ confidence interval search. If no confidence bounds could be determined no value is given.

Active layer	PBDB-T:ITIC			PBT7-Th:PCBM		
[nm]	Munich	Sweden	Space	Munich	Sweden	Space
Large domain	89–4 + 4	61–11 + 14	92–23 + 4	84–5 + 7	62–7 + 5	90–1 + 10
Middle domain	32–5 + 3	23±3	30–1 + 4	16±2	22–3 + 2	30–3 + 8
Small domain	1.8	1.9	1.3 + 0.4	1.0–0 + 0.3	2.0–0.1 + 0.2	1.0 + 0.4

relative number of large domains is much lower for the space sample compared to the Munich sample. In the horizontal line cuts, one can accordingly see in Figure 5d how a broad region of a single power law for intermediate q_y values forms a buckled curve for the Sweden sample, where after the rocket flight and oxygen exposure the buckle spreads out, that is, toward a broader domain size distribution. The evolution from Munich over Sweden to space does not follow a directed trend, in particular, the middle-sized domains appear to increase first in relative number for Sweden and grow and flatten out for the space sample. There seem to be concurring mechanisms present that would need further investigation to disentangle transport and flight influence for the space SCs.

Since the morphology undergoes changes during transport to Sweden or during the rocket flight to space, it is of interest if there are also changes to the structure on a smaller scale, that is, to the crystalline regions of the active layers. Therefore, the crystalline structure is probed with GIWAXS. GIWAXS data are shown in Figure 7 for the mesoporous TiO_2 perovskite

SCs. An identical analysis can be found in Figure S5, Supporting Information, for the planar SnO_2 perovskite SCs.

No crystal structure changes are visible for the perovskite SCs. The pseudo-X-ray diffractogram reveals a phase-pure perovskite with only a minor PbI_2 side phase (Figure 7a). Neither do Bragg peak intensities change from reference samples to space samples nor are significant changes in the peak FWHM maxima observed for the Bragg peaks. Also, the crystal orientation of the perovskite phase and PbI_2 phase with respect to the electrodes exhibits no noticeable differences (Figure 7b,c). For mixed halide mixed cation perovskite SCs, related to Guo et al., the breaking of small crystals was attributed to a strain release and linked with the demixing of the perovskite phase.^[40] However, in the present study, phase segregation can be ruled out because this would become visible in the 2D GIWAXS data (Figure S4, Supporting Information) and the Pseudo X-ray diffractograms. As suggested by GISAXS, the relative reduction of large domain numbers and increase of small domain numbers in the perovskite did not result in measurable changes in the crystal phase as accessed in GIWAXS.

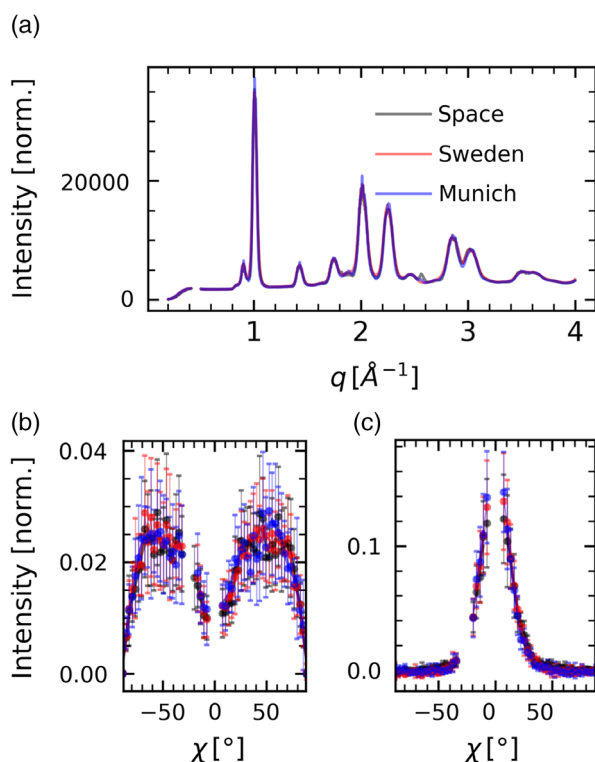


Figure 7. Analysis of the crystalline part of the TiO_2 perovskite SCs: a) Pseudo X-Ray diffractogram of all three samples, intensity normalized to the low- q range. b) Radially integrated azimuthal tube cut of the (001) perovskite Bragg peak, which is the strongest peak in the diffractogram, including local background subtraction with area normalization. c) Radially integrated azimuthal tube cut of the PbI_2 reflex with the same treatment.

The silver conductive paste used to aid electrode contacting is known to be detrimental to the long-term stability of perovskite SCs, since silver diffuses inside the perovskite, triggering chemical degradation of the perovskite.^[60] However, we did not observe any degradation, possibly due to vacuum exposure where solvent removal could constrain the mobility of silver atoms, the small amount used, or simply the too-short time for significant silver diffusion.

For the organic SCs, the overview of resulting q -maps measured in GIWAXS to probe their crystallinity can be seen in Figure S4, Supporting Information, for the PTB7-Th:PCBM and PBDB-T:ITIC active layers at an incident angle of 0.4° . The extracted line cuts are presented in Figure S6, Supporting Information, respectively. From the graphs, similarly, as for the perovskite SCs, no obvious changes in the crystalline structure can be identified. We note that the measurements presented here with the incident angle of 0.4° are not particularly sensitive to organic crystallinity but rather probe the inorganic part of high crystallinity. Thus, the measurements in this geometry indicate no significant changes in crystallinity in the SC inorganic layers. Therefore, we also performed measurements around the critical angle of the active layer at 0.12° incident angle to probe the crystallinity of the bulk-heterojunction with a stronger scattering signal from the polymer:small molecule layer. The resulting q -maps can be found in Figure S7, Supporting Information, with a focus on

the region within $q \approx 2 \text{ \AA}^{-1}$. Apparently, from closer inspection of the inner q -region at around 0.3 – 0.5 , and 1.3 – 1.7 \AA^{-1} crystalline signal of the polymer bulk-heterojunctions can be found.^[61,62] To assess the differences between the Munich, Sweden, and space samples in more detail, out-of-plane and in-plane sector cuts are shown in Figure 8 for PTB7-Th:PCBM and accordingly for PBDB-T:ITIC in Figure S8, Supporting Information.

Focusing on the in-plane azimuthally integrated radial sector cuts for PTB7-Th:PCBM organic SCs, no polymer signal is observed at around 0.3 \AA^{-1} . The Munich, Sweden, and space measurement intensity trends do not show any pronounced differences in the range of interest up to $\approx 1.5 \text{ \AA}^{-1}$. For the space sample, the crystalline polymer signal of the (100) Bragg peak of PTB7-Th including higher orders appears, while this cannot be found for the reference samples. The broad amorphous peak of PCBM is located at around 1.3 \AA^{-1} and seems to be increasing in intensity from Munich over Sweden to the space sample.^[62] The increased Bragg signal of PTB7-Th is a result of the ordering of the PTB7-Th by a face-on sheet stacking, which is accompanied by an increased amorphous scattering signal arising from the PCBM-phases. These findings show a demixing of the polymer blend, while for the Sweden sample, minor stacking changes occur, only indicating a mild PCBM-signal increase. For the space sample, polymer sheet stacking pronounces the signal more strongly, leading to the appearance of higher Bragg-reflex orders. The PCBM scattering signal is increased simultaneously, showing aggregation and demixing of the bulk-heterojunction

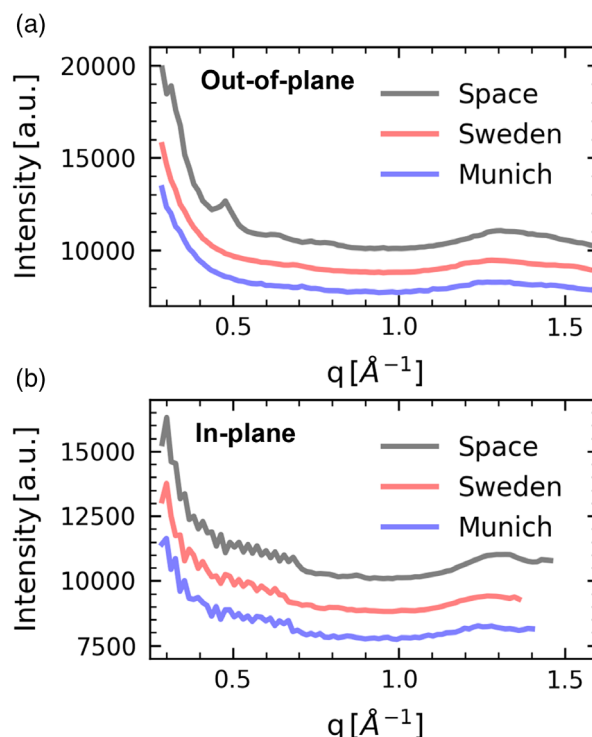


Figure 8. Analysis of the crystalline part of the PTB7-Th:PCBM organic SCs from GIWAXS measurements at 0.12° incident angle: a) out-of-plane azimuthally integrated radial sector cut and b) in-plane azimuthally integrated radial sector cut.

blend, which is undesired for organic photovoltaics using such a blend system.^[63]

The 2D GIWAXS data of the PBDB-T:ITIC organic SCs measured at 0.12° show PBDB-T (100) Bragg reflexes at $\approx 0.3 \text{ \AA}^{-1}$ for all three samples, the Munich reference, the Sweden reference, and the space SCs (Figure S7, Supporting Information).^[61] This intrinsic polymer crystallinity is present for all the samples in the form of a primarily isotropic ring, apart from the out-of-plane direction where the SAXS region overlays. The space sample is in this regard the only sample that shows a weak second-order peak in out-of-plane direction at $\approx 0.55 \text{ \AA}^{-1}$, which cannot be found for the Munich and Sweden reference samples. Here, we note that the intensity of the polymer peaks for the Sweden reference sample is not comparable to the Munich or space sample due to enhanced air scattering. However, the features follow the trend as best visible in Figure S6, Supporting Information. Comparing the Munich and space SCs in the out-of-plane sector cuts, the ITIC amorphous peak found at around 1.7 \AA^{-1} shows similar intensities. Nevertheless, for the space SC, the q position of the peak increases, indicative of a smaller ITIC crystal lattice spacing. This finding indicates slight phase segregation where ITIC pure phases assemble in denser packing, while the PBDB-T second-order reflex indicates slightly increased phase segregation in the blend.

Combining the findings from the X-ray characterization with GISAXS and GIWAXS, a complex scenario is found for the processes that influence the active layer of the perovskite and organic SCs during travel and spaceflight. Interestingly, the travel from Munich to Sweden and back alone slightly changed the SCs' morphology. Especially, the organic materials respond with minor changes in their domain size distribution. In the nonfullerene PBDB-T:ITIC system, the travel appears to reduce the size of the intermediate structures but to increase their relative number, while larger structures remain unaltered. In the fullerene PBT7-Th:PCBM system, there appears to be a subtle increase in amorphous PCBM content as seen in GIWAXS upon travel. GISAXS shows a number reduction of intermediate structures and a number increase of large structures. Typically, such agglomeration effects are not desirable since domains grow too large to sustain efficient exciton transfer and separation anymore. In contrast, the perovskite SCs show more subtle changes in their morphology, where the number of small domains increases compared to the number of large domains. However, the crystal phases of all SC types are stable without measurable changes in GIWAXS for the stationary and travel SCs.

Focusing now on the space SCs, the perovskite space samples continue the trend of domain polydispersity being shifted toward a higher number of smaller domains while the crystal phase remains stable without observed changes. The organic space samples, however, show a slight increase in polymer crystallinity in GIWAXS, which suggests a mild demixing and aggregation of the blend after exposure to space conditions and environmental conditions. The morphological changes of the PBDB-T:ITIC active layer support this finding with the growth of intermediate-size domains, while large, probably well-mixed domains decrease in their number. In contrast to this, there is no significant change of morphology from travel to spaceflight of the PBT7-Th:PCBM active layer. Slight PCBM demixing first reduces the domain size of the blend where thereafter space and

environmental exposure, for example, the abundance of oxygen, accelerate PBT7-Th stacking, which slightly increases the observed domain sizes in GISAXS. However, the latter effect is not strong and further studies will be required to disentangle the different processes occurring in different environments more precisely.

To assess the reason for changes during travel to Sweden, we speculate in the following by listing several possibilities that could influence the SC morphology and crystal structure. Influences due to cosmic radiation during airplane travel are possible but unlikely to cause such significant changes. Also, in such a case, the expectation would be to identify radiation effects in GIWAXS more than in GISAXS, because the former is sensitive to the crystal phase on the nanometer scale. Alternatively, tiny amounts of oxygen in the sealed bags or not being perfectly diffusion-proof in combination with pressure differences during take-off and landing of the airplane could play a role for the Sweden reference SCs. However, the bag protection seems sufficient to maintain stable crystal phases for all SC systems, and also the nitrogen-filled glovebox is not completely oxygen-free. Also, there could be some solvent traces or other volatile species present that act in the sealed bags and lead to a kind of solvent posttreatment, especially since the perovskite and organic SCs have been packaged inside one single bag, enabling some cross-effects to take place. Traces of residual solvent were reported in the literature for perovskite and organic SCs and could promote mobility inside the active layer to introduce morphology changes.^[64,65] Future studies would be necessary to separate the influence of such different effects, which would affect every transport of perovskite and organic SCs.

5. Conclusion

In this work, we give a detailed photovoltaic characterization overview of the spaceflight of perovskite and organic SCs on a sounding rocket. We complete a detailed irradiance-based performance analysis by relating SC performance to reconstructed solar irradiance. All four SC types show reasonable PCE values ranging from 5% to 13%. These encouraging results are based on a conservative estimate and are reached despite all measurements carried out in exotic experimental circumstances in space conditions. Apart from geometrical effects at low irradiances, there is a positive correlation between SC performance with irradiance, especially for perovskite SCs. This difference is mainly attributed to the increasing V_{oc} values for increasing irradiances for perovskite SCs within the irradiance range of up to ≈ 1.1 sun, while V_{oc} values of organic SCs tend to level off above 0.6 sun. The short-current density seems to increase more than linearly for increasing irradiances, which cannot be solely attributed to geometrical or shadowing effects. With the time of the rocket flight in space, the V_{oc} values decline slightly and FF values decline moderately which is correlated to increasing SC temperatures due to thermal conduction or radiation from the hot mantle surface to the inside.

During the rocket flight, the SCs were exposed to ultra-high vacuum, temperatures ranging from 20 to 65 °C, and strong solar irradiation of more than 1 sun. However, soot on the exterior window has blocked parts of the intense UV radiation.

The retrieved space SCs have been brought back for a postspace-flight characterization using GISAXS/GIWAXS to study potential changes in their morphology and crystal structure. Importantly, the travel from Munich to Sweden and back alone changed somewhat the morphology of the active layers. Regarding the SCs exposed to environmental conditions during the rocket flight, the fullerene system shows no significant results, while the small-acceptor system experiences a slight coarse-graining of intermediate structures and a reduction of large structures. The perovskite SCs show clear but small changes of reduction of the relative number of large domains and a number increase of small domains. In contrast to these changes in the active layer morphology on the nanoscale, the crystalline structure does not show significant differences for any of the studied SC types. In this regard, the perovskite SCs do not show any sign of changes, and the organic SCs remain unaltered during space travel. Notably, the observed changes in the morphology of the travel SCs, which presumably are experienced similarly for the space SCs, do not cause a failure of the latter. Slight increases in organic crystallinity are likely attributed to gentle demixing of the bulk-heterojunction blends, which can be attributed to environmental effects during and after the spaceflight. Thus, neither the travel to the rocket launching site in Sweden nor the harsh rocket launch or the short stay in space as well as the Earth's atmosphere reentry, prevent the organic and perovskite SCs from functioning with satisfactory quality. These findings are highly promising for moving forward and studying these next-generation SCs in future flights to space with a more detailed postcharacterization study and for longer time durations in space to investigate long-term aging under real space conditions.

6. Experimental Section

Sample Transport and Storage Conditions: After sample fabrication in N₂-filled gloveboxes (details see in Reb et al.^[48]), some reference SCs were left in Munich inside the glovebox (denoted the Munich SCs) while several packages of sealed SC mounting batches were carried by airplane flight in the hand luggage to the rocket launch site in Kiruna, Northern Sweden. There, the SC packages were stored at room temperature for around 10 days. Here, we note that the different SC types were stored in common bags, that is, they were not separated according to their type.

Several hours before launch, the space SCs were unpacked from their light-proof packaging in protective nitrogen atmosphere to mount them in the experiment avoiding light exposure. During mounting, tiny drops of silver conductive paste were added with a fine brush to the contact pin area to ensure a stable electrical connection several millimeters away from the aperture area. The reference SCs in Sweden remained in their protective nitrogen atmosphere (denoted the Sweden SCs).

After flight and reentry, the payload landed safely on dry solid ground in a parachute descent and was recovered by helicopter within a few hours. The space SCs experienced, including the time before launch, around 8 h of ambient conditions of 15–20 °C with <≈30% relative humidity. Then, the SCs were recovered, with no sign of any visual degradation. After recovering the SCs, they were packed together and due to the lack of nitrogen, partly evacuated with a vacuum sealer machine. After traveling back to Munich by airplane in hand luggage, the space SCs and the Sweden reference cells were brought back into the laboratory gloveboxes. After repacking the Munich reference, Sweden reference, and space SCs in nitrogen-filled bags they were carried by train to DESY, Hamburg, for the X-ray measurements.

X-Ray Characterization: Grazing-incidence X-ray scattering was performed at the PETRA III synchrotron P03 beamline, where

grazing-incidence small-angle X-ray scattering (GISAXS) and grazing-incidence wide-angle X-ray scattering (GIWAXS) was measured on the SCs.^[66] To avoid detector saturation, the SCs were probed in between the metal electrodes in the vicinity of the active area. A beam of $23 \times 32 \mu\text{m}^2$ shape with a monochromatic X-ray energy of 12.9 keV (corresponding to 0.961 Å) with a high brilliance impinged the samples at an incidence angle of 0.4°, which is above the critical angle of the involved materials, to probe the buried morphology and crystal structure in the bulk active layer of the SCs. This angle was used for all measurements of the perovskite SCs and for GISAXS measurements of the organic SCs; for GIWAXS measurements of the organic SCs, we maximized the active layer crystalline signal by scanning the incident angle and found the strongest signal for 0.12°, above the typical critical angle of the used polymers.^[67,68] Thus, the presented measurements are all probing the bulk film and are not specifically surface sensitive. For GISAXS, a Dectris Pilatus 1M detector was used behind a vacuumed flight tube at a distance of 2,701 mm. For GIWAXS, a Dectris Pilatus 300 k detector was positioned at a distance of about 116 mm. Data reduction was performed with the software INSIGHT,^[69] including typical GIWAXS geometrical and intensity corrections (solid-angle correction, detector pixel sensitivity correction, polarization correction, and air attenuation correction). Since the footprint on top of the sample can move a distance of several mm, for GIWAXS analysis, an individual correction of the sample-detector distance was performed. For the perovskite SCs, the (001) MAFA perovskite ring was corrected to $q = 1.0089 \text{ nm}^{-1}$.^[70] The known ITO peak position was used for correction for the organic SCs.^[71] A Si attenuation of 3.50 mm^{-1} and a horizontal polarization of 0.98 was used, and an air attenuation coefficient of $3.01 \times 10^{-4} \text{ mm}^{-1}$ was used for GIWAXS.^[72]

Scattering Data Reduction: All the GISAXS and GIWAXS data were reduced with the software INSIGHT.^[69] For analysis of the GISAXS data, vertical and horizontal line cuts were performed. An angular width of 0.02°, corresponding to six pixels, was used for the vertical line cuts. To maximize the signal arising from the polymer bulk-heterojunction active layer, the horizontal line cut was performed around the critical angle of the polymer^[67,68] within 0.095–0.115°, resulting in a cut-width of 6 px, from which the arithmetic mean including standard deviation was determined for each pixel row.

The resulting line cut data was folded onto one side and then modeled in the framework of the distorted-wave Born approximation (DWBA) and the local monodisperse approximation (LMA) of three decoupled cylindrical form factors in a 1D paracrystalline structure, making use of the effective interface approximation.^[68] For the form factor sizes and the structure distance, normal distributions were included in the DWBA-based LMA. For the modeling of the perovskite SCs, no structure factor was assumed, that is, no further assumptions for the lateral distribution of the domains were needed.^[73] The standard deviation of the size distribution of the form factors was fixed at $\sigma = 0.7 \text{ R}$ for the perovskite SCs. For the modeling of the organic SCs, structure factors were required to describe the measured data with the model. Where possible, the form factor standard deviation was fixed to similar values to maximize the comparability of the resulting model parameter values. As explained in earlier work, the number of scattering centers contributing to the respective GISAXS signal and the relative number of scattering centers were calculated from the model fits.^[73] For the analysis of the GIWAXS data, radially integrated azimuthal tube cuts and azimuthally integrated radial sector cuts were performed in the q_i – q_z plane. For the perovskite SCs, tube cuts of the (001) perovskite Bragg peaks were performed by cutting the central 1 sigma of the perovskite reflex and locally subtracting the intensity average of an inner and outer ring with 0.5 sigma width in a distance to the reflex center of 2.5 sigma on an angular grid of 60 points. For the PbI₂ Bragg peak, the central intensity within 1 sigma was locally subtracted with inner/outer annuli with a width of 0.5 sigma at a distance of 1.5 sigma to the center. The resulting tube cuts were normalized to unity area. A half-circle sector cut that covered all scattering intensity (pseudo-XRD^[71]) was performed and binned for further analysis. The resulting line-cuts were intensity normalized in the region 0.6–0.7 nm^{−1} where the data appeared flat and no significant features were in the vicinity, except stated differently. For the

organic SCs, sector cuts in out-of-plane (sample-plane) direction from -25° to $+25^\circ$ and in in-plane direction from 55° to 85° have been performed.

UV-Vis Measurements: UV-vis measurements were done with a Perkin Elmer Lambda 35 in a wavelength range from 280 to 1100 nm with a scan speed of 480 nm min^{-1} with a bandwidth of 1 nm with 5 nm measurement steps.

Supporting Information

Supporting Information is available from the Wiley Online Library or from the author.

Acknowledgements

This work was supported by funding from Deutsche Zentrum für Luft- und Raumfahrt e.V. (DLR) grant number 50WM2256, the Deutsche Forschungsgemeinschaft (DFG, German Research Foundation) grant number Mu1487/22, and by International Research Training Group 2022 Alberta/Technical University of Munich International Graduate School for Environmentally Responsible Functional Materials (ATUMS) as well as from TUM.solar in the context of the Bavarian Collaborative Research Project "Solar Technologies Go Hybrid" (SolTech). We thank the department Mobile Rocket Base (MORABA) of the DLR Space Operations and Astronaut Training for the support and guidance during the project. R.G. acknowledges the China Scholarship Council (CSC). Parts of this research were carried out at the light source PETRA III at DESY, a member of the Helmholtz Association (HGF).

Open Access funding enabled and organized by Projekt DEAL.

Conflict of Interest

The authors declare no conflict of interest.

Data Availability Statement

The data that support the findings of this study are available from the corresponding author upon reasonable request.

Keywords

morphology, organic solar cells, perovskite solar cells, rocket flight, space

Received: January 31, 2023

Published online: February 23, 2023

- [1] M. A. Green, E. D. Dunlop, J. Hohl-Ebinger, M. Yoshita, N. Koidakis, K. Bothe, D. Hinken, M. Rauer, X. Hao, *Progr. Photovolt.* **2022**, *30*, 687.
- [2] NREL, Best Research-Cell Efficiencies, <https://www.nrel.gov/pv/cell-efficiency.html> (accessed: February 2022).
- [3] L. Zhan, S. Li, Y. Li, R. Sun, J. Min, Y. Chen, J. Fang, C.-Q. Ma, G. Zhou, H. Zhu, L. Zuo, H. Qiu, S. Yin, H. Chen, *Adv. Energy Mater.* **2022**, *12*, 2201076.
- [4] J. Y. Kim, J.-W. Lee, H. S. Jung, H. Shin, N.-G. Park, *Chem. Rev.* **2020**, *120*, 7867.
- [5] P. Müller-Buschbaum, M. Thelakkat, T. F. Fässler, M. Stutzmann, *Adv. Energy Mater.* **2017**, *7*, 1700248.
- [6] R. Sun, W. Wang, H. Yu, Z. Chen, X. Xia, H. Shen, J. Guo, M. Shi, Y. Zheng, Y. Wu, W. Yang, T. Wang, Q. Wu, Y. Yang, X. Lu, J. Xia, C. J. Brabec, H. Yan, Y. Li, J. Min, *Joule* **2021**, *5*, 1548.
- [7] Y. Li, X. Huang, K. Ding, H. K. M. Sheriff, L. Ye, H. Liu, C.-Z. Li, H. Ade, S. R. Forrest, *Nat. Commun.* **2021**, *12*, 5419.
- [8] L.-H. Chou, J. M. W. Chan, C.-L. Liu, *Sol. RRL* **2022**, *6*, 2101035.
- [9] J. Li, J. Dagar, O. Shargaieva, M. A. Flatken, H. Köbler, M. Fenske, C. Schultz, B. Stegemann, J. Just, D. M. Többsens, A. Abate, R. Munir, E. Unger, *Adv. Energy Mater.* **2021**, *11*, 2003460.
- [10] Y. Galagan, F. Di Giacomo, H. Gorter, G. Kirchner, I. de Vries, R. Andriessen, P. Groen, *Adv. Energy Mater.* **2018**, *8*, 1801935.
- [11] Q. Wu, J. Guo, R. Sun, J. Guo, S. Jia, Y. Li, J. Wang, J. Min, *Nano Energy* **2019**, *61*, 559.
- [12] N. Rolston, W. J. Scheideler, A. C. Flick, J. P. Chen, H. Elmaraghi, A. Sleugh, O. Zhao, M. Woodhouse, R. H. Dauskardt, *Joule* **2020**, *4*, 2675.
- [13] X. Jiang, P. Chotard, K. Luo, F. Eckmann, S. Tu, M. A. Reus, S. Yin, J. Reitenbach, C. L. Weindl, M. Schwartzkopf, S. V. Roth, P. Müller-Buschbaum, *Adv. Energy Mater.* **2022**, *12*, 2103977.
- [14] S. Pescetelli, A. Agresti, G. Viskadourous, S. Razza, K. Rogdakis, I. Kalogerakis, E. Spiliarotis, E. Leonardi, P. Mariani, L. Sorbello, M. Pierro, C. Cornaro, S. Bellani, L. Najafi, B. Martín-García, A. E. Del Rio Castillo, R. Oropesa-Núñez, M. Prato, S. Maranghi, M. L. Parisi, A. Sinicropi, R. Basosi, F. Bonaccorso, E. Kymakis, A. Di Carlo, *Nat. Energy* **2022**, *7*, 597.
- [15] J. Wu, P. Chen, H. Xu, M. Yu, L. Li, H. Yan, Y. Huangfu, Y. Xiao, X. Yang, L. Zhao, W. Wang, Q. Gong, R. Zhu, *Sci. China Mater.* **2022**, *65*, 2319.
- [16] C. G. Reynolds, C. M. Green, V. Lomask, *Military Affairs* **1971**, *35*, 120.
- [17] M. T. Hoang, Y. Yang, B. Tuten, H. Wang, *J. Phys. Chem. Lett.* **2022**, *13*, 2908.
- [18] N. S. Fatemi, H. E. Pollard, H. Q. Hou, P. R. Sharps, in Conf. Record of the Twenty-Eighth IEEE Photovoltaic Specialists Conf.- 2000, IEEE, Piscataway, NJ, pp. 1083–1086.
- [19] D. Cardwell, A. Kirk, C. Stender, A. Wibowo, F. Tuminello, M. Drees, R. Chan, M. Osowski, N. Pan, in 2017 IEEE 44th Photovoltaic Specialists Conf. (PVSC), IEEE, Piscataway, NJ **2017**, pp. 3511–3513.
- [20] M. Kaltenbrunner, M. S. White, E. D. Glowacki, T. Sekitani, T. Someya, N. S. Sariciftci, S. Bauer, *Nat. Commun.* **2012**, *3*, 770.
- [21] Y. Li, L. Meng, Y. M. Yang, G. Xu, Z. Hong, Q. Chen, J. You, G. Li, Y. Yang, Y. Li, *Nat. Commun.* **2016**, *7*, 10214.
- [22] T. Kim, J.-H. Kim, T. E. Kang, C. Lee, H. Kang, M. Shin, C. Wang, B. Ma, U. Jeong, T.-S. Kim, B. J. Kim, *Nat. Commun.* **2015**, *6*, 8547.
- [23] M. Kaltenbrunner, G. Adam, E. D. Glowacki, M. Drack, R. Schwödiauer, L. Leonat, D. H. Apaydin, H. Groiss, M. C. Scharber, M. S. White, N. S. Sariciftci, S. Bauer, *Nat. Mater.* **2015**, *14*, 1032.
- [24] S. Kang, J. Jeong, S. Cho, Y. J. Yoon, S. Park, S. Lim, J. Y. Kim, H. Ko, *J. Mater. Chem A* **2019**, *7*, 1107.
- [25] W. Huang, Z. Jiang, K. Fukuda, X. Jiao, C. R. McNeill, T. Yokota, T. Someya, *Joule* **2020**, *4*, 128.
- [26] F. Lang, G. E. Eperon, K. Frohna, E. M. Tennyson, A. Al-Ashouri, G. Kourkafas, J. Bundesmann, A. Denker, K. G. West, L. C. Hirst, H.-C. Neitzert, S. D. Stranks, *Adv. Energy Mater.* **2021**, *11*, 2102246.
- [27] A. F. Palmstrom, G. E. Eperon, T. Leijtens, R. Prasanna, S. N. Habisreutinger, W. Nemeth, E. A. Gauding, S. P. Dunfield, M. Reese, S. Nanayakkara, T. Moot, J. Werner, J. Liu, B. To, S. T. Christensen, M. D. McGehee, M. F. van Hest, J. M. Luther, J. J. Berry, D. T. Moore, *Joule* **2019**, *3*, 2193.
- [28] E. N. Güler, A. Distler, R. Basu, C. J. Brabec, H.-J. Egelhaaf, *Flex. Print. Electron.* **2022**, *7*, 25003.
- [29] R. Thirsk, A. Kuipers, C. Mukai, D. Williams, *Canadian Med. Assoc. J.* **2009**, *180*, 1216.
- [30] M. A. Green, *Progr. Photovolt.* **2012**, *20*, 954.
- [31] NREL, 2000 ASTM Standard Extraterrestrial Spectrum Reference E-490-00, <https://www.nrel.gov/grid/solar-resource/spectra-astm-e490.html> (accessed: February 2022).

- [32] S. Guo, C. Brandt, T. Andreev, E. Metwalli, W. Wang, J. Perlich, P. Müller-Buschbaum, *ACS Appl. Mater. Interfaces* **2014**, 6, 17902.
- [33] C. Chen, H. Li, J. Jin, X. Chen, Y. Cheng, Y. Zheng, D. Liu, L. Xu, H. Song, Q. Dai, *Adv. Energy Mater.* **2017**, 7, 1700758.
- [34] J. Barbé, D. Hughes, Z. Wei, A. Pockett, H. K. H. Lee, K. C. Heasman, M. J. Carnie, T. M. Watson, W. C. Tsoi, *Sol. RRL* **2019**, 3, 1900219.
- [35] F. Lang, N. H. Nickel, J. Bundesmann, S. Seidel, A. Denker, S. Albrecht, V. V. Brus, J. Rappich, B. Rech, G. Landi, H. C. Neitzert, *Adv. Mater* **2016**, 28, 8726.
- [36] G. M. Paternò, V. Robbiano, K. J. Fraser, C. Frost, V. García Sakai, F. Cacialli, *Sci. Rep.* **2017**, 7, 41013.
- [37] G. Li, Y. Yang, R. A. B. Devine, C. Mayberry, *Nanotechnology* **2008**, 19, 424014.
- [38] Y. Miyazawa, M. Ikegami, H.-W. Chen, T. Ohshima, M. Imaizumi, K. Hirose, T. Miyasaka, *iScience* **2018**, 2, 148.
- [39] A. R. Kirmani, B. K. Durant, J. Grandier, N. M. Haegel, M. D. Kelzenberg, Y. M. Lao, M. D. McGehee, L. McMillon-Brown, D. P. Ostrowski, T. J. Peshek, B. Rout, I. R. Sellers, M. Steger, D. Walker, D. M. Wilt, K. T. VanSant, J. M. Luther, *Joule* **2022**, 6, 1015.
- [40] R. Guo, D. Han, W. Chen, L. Dai, K. Ji, Q. Xiong, S. Li, L. K. Reb, M. A. Scheel, S. Pratap, N. Li, S. Yin, T. Xiao, S. Liang, A. L. Oechsle, C. L. Weindl, M. Schwartzkopf, H. Ebert, P. Gao, K. Wang, M. Yuan, N. C. Greenham, S. D. Stranks, S. V. Roth, R. H. Friend, P. Müller-Buschbaum, *Nat. Energy* **2021**, 6, 977.
- [41] Y. Bai, Z. Huang, X. Zhang, J. Lu, X. Niu, Z. He, C. Zhu, M. Xiao, Q. Song, X. Wei, C. Wang, Z. Cui, J. Dou, Y. Chen, F. Pei, H. Zai, W. Wang, T. Song, P. An, J. Zhang, J. Dong, Y. Li, J. Shi, H. Jin, P. Chen, Y. Sun, Y. Li, H. Chen, Z. Wei, H. Zhou, Q. Chen, *Science* **2022**, 378, 747.
- [42] R. Cheacharoen, N. Rolston, D. Harwood, K. A. Bush, R. H. Dauskardt, M. D. McGehee, *Energy Environ. Sci.* **2018**, 11, 144.
- [43] I. Z. C. Bautista, S. Yang, A. Kuyyakanont, M. Iwata, T. Ma, M. Cho, *Trans. Japan Soc. Aero. S Sci.* **2022**, 65, 95.
- [44] D. Hughes, S. M. P. Meroni, J. Barbé, D. Raptis, H. K. H. Lee, K. C. Heasman, F. Lang, T. M. Watson, W. C. Tsoi, *Energy Technol.* **2021**, 9, 2100928.
- [45] I. Cardinaletti, T. Vangerven, S. Nagels, R. Cornelissen, D. Schreurs, J. Hruby, J. Vodnik, D. Devisscher, J. Kesters, J. D'Haen, A. Franquet, V. Spampinato, T. Conard, W. Maes, W. Deferme, J. V. Manca, *Sol. Energy Mater. Sol. Cells* **2018**, 182, 121.
- [46] Y. Tu, G. Xu, X. Yang, Y. Zhang, Z. Li, R. Su, D. Luo, W. Yang, Y. Miao, R. Cai, L. Jiang, X. Du, Y. Yang, Q. Liu, Y. Gao, S. Zhao, W. Huang, Q. Gong, R. Zhu, *Sci. China Phys., Mech. Astronomy* **2019**, 62, 974221.
- [47] H. Wang, X. Jiang, Y. Cao, L. Qian, Y. Liu, M. Huang, C. Zhang, Y. Hao, K. Wang, S. Liu, *Adv. Energy Mater.* **2022**, 13, 2202643.
- [48] L. K. Reb, M. Böhmer, B. Predeschly, S. Grott, C. L. Weindl, G. I. Ivandekic, R. Guo, C. Dreißigacker, R. Gernhäuser, A. Meyer, P. Müller-Buschbaum, *Joule* **2020**, 4, 1880.
- [49] L. K. Reb, M. Böhmer, B. Predeschly, S. Grott, C. Dreißigacker, J. Drescher, A. Meyer, P. Müller-Buschbaum, *Rev. Sci. Instrum.* **2021**, 92, 74501.
- [50] L. K. Reb, M. Böhmer, B. Predeschly, L. V. Spanier, C. Dreißigacker, A. Meyer, P. Müller-Buschbaum, *Sol. RRL* **2022**, 6, 2200537.
- [51] B. Braun, J. Barf, *CEAS Space J.*, <https://link.springer.com/article/10.1007/s12567-022-00461-0>.
- [52] M. Saliba, J.-P. Correa-Baena, C. M. Wolff, M. Stolterfoht, N. Phung, S. Albrecht, D. Neher, A. Abate, *Chem. Mater.* **2018**, 30, 4193.
- [53] S.-H. Liao, H.-J. Jhuo, P.-N. Yeh, Y.-S. Cheng, Y.-L. Li, Y.-H. Lee, S. Sharma, S.-A. Chen, *Sci. Rep.* **2014**, 4, 6813.
- [54] N. Y. Doumon, M. V. Dryzhov, F. V. Houard, V. M. Le Corre, A. Rahimi Chatri, P. Christodoulis, L. J. A. Koster, *ACS Appl. Mater. Interfaces* **2019**, 11, 8310.
- [55] M. Jošt, B. Lipovšek, B. Glazar, A. Al-Ashouri, K. Brecl, G. Matič, A. Magomedov, V. Getautis, M. Topič, S. Albrecht, *Adv. Energy Mater.* **2020**, 10, 2000454.
- [56] N. Bristow, J. Kettle, *J. Renew. Sustain. Energy* **2015**, 7, 13111.
- [57] W. Shockley, H. J. Queisser, *J. Appl. Phys.* **1961**, 32, 510.
- [58] P. Müller-Buschbaum, *Adv. Mater* **2014**, 26, 7692.
- [59] J. Schlipf, P. Müller-Buschbaum, *Adv. Energy Mater.* **2017**, 7, 1700131.
- [60] S. Svanström, T. J. Jacobsson, G. Boschloo, E. M. J. Johansson, H. Rensmo, U. B. Cappel, *ACS Appl. Mater. Interfaces* **2020**, 12, 7212.
- [61] S. Grott, A. Kotobi, L. K. Reb, C. L. Weindl, R. Guo, S. Yin, K. S. Wienhold, W. Chen, T. Ameri, M. Schwartzkopf, S. V. Roth, P. Müller-Buschbaum, *Sol. RRL* **2022**, 6, 2101084.
- [62] D. E. Johnston, K. G. Yager, H. Hlaing, X. Lu, B. M. Ocko, C. T. Black, *ACS Nano* **2014**, 8, 243.
- [63] C. J. Schaffer, C. M. Palumbiny, M. A. Niedermeier, C. Burger, G. Santoro, S. V. Roth, P. Müller-Buschbaum, *Adv. Energy Mater.* **2016**, 6, 1600712.
- [64] D. M. Schwaiger, W. Lohstroh, P. Müller-Buschbaum, *Macromolecules* **2021**, 54, 6534.
- [65] Z. Xiao, Q. Dong, C. Bi, Y. Shao, Y. Yuan, J. Huang, *Adv. Mater.* **2014**, 26, 6503.
- [66] A. Buffet, A. Rothkirch, R. Döhrmann, V. Körstgens, M. M. Abul Kashem, J. Perlich, G. Herzog, M. Schwartzkopf, R. Gehrke, P. Müller-Buschbaum, S. V. Roth, *J. Synchrotr. Radiat.* **2012**, 19, 647.
- [67] Y. Yoneda, *Phys. Rev.* **1963**, 131, 2010.
- [68] G. Renaud, R. Lazzari, F. Leroy, *Surf. Sci. Rep.* **2009**, 64, 255.
- [69] M. A. Reus, L. K. Reb, Insight: The in-situ GIXS heuristic tool for efficient reduction of grazing-incidence scattering data, <https://www.ph.nat.tum.de/functmat/forschung/insight/> (accessed: February 2023).
- [70] L.-Q. Xie, L. Chen, Z.-A. Nan, H.-X. Lin, T. Wang, D.-P. Zhan, J.-W. Yan, B.-W. Mao, Z.-Q. Tian, *J. Am. Chem. Soc.* **2017**, 139, 3320.
- [71] Y. Shigesato, R. Koshi-ishi, T. Kawashima, J. Ohsako, *Vacuum* **2000**, 59, 614.
- [72] Tables of X-Ray Mass Attenuation Coefficients and Mass Energy-Absorption Coefficients, NIST Standard Reference Database, **1995**, p. 126, <https://dx.doi.org/10.18434/T4D01F>.
- [73] J. Schlipf, P. Docampo, C. J. Schaffer, V. Körstgens, L. Bießmann, F. Hanusch, N. Giesbrecht, S. Bernstorff, T. Bein, P. Müller-Buschbaum, *J. Phys. Chem. Lett.* **2015**, 6, 1265.